Combining finite element and finite volume methods for efficient multiphase flow simulations in highly heterogeneous and structurally complex geologic media

Author(s):
Geiger, Sebastian; Roberts, Steven; Matthäi, Stephan K.; Zoppou, Christopher; Burri, Adrian

Publication date:
2004-11

Permanent link:
https://doi.org/10.3929/ethz-b-000160244

Originally published in:
Geofluids 4(4), https://doi.org/10.1111/j.1468-8123.2004.00093.x

Combining finite element and finite volume methods for efficient multiphase flow simulations in highly heterogeneous and structurally complex geologic media

Sebastian Geiger [*] Steven Roberts [†] Stephan K. Matthäi [‡]
Christopher Zoppou [§] Adrian Burri [¶]

October 21, 2004

Abstract

The permeability of the Earth's crust commonly varies over many orders of magnitude. Flow velocity can range over several orders of magnitude in structures of interest that vary in scale from centimeters to kilometers. To accurately and efficiently model multiphase flow in geologic media, we introduce a fully conservative node-centered finite volume method coupled with a Galerkin finite element method on an unstructured triangular grid with a complementary finite volume subgrid. The effectiveness of this approach is demonstrated by comparison with traditional solution methods and by multiphase flow simulations for heterogeneous permeability fields including complex geometries that produce transport parameters and lengths scales varying over four orders of magnitude.

Keywords: Finite Volumes, Finite Elements, TVD, Multiphase Flow, Fractures, Porous Media, Heterogeneity

Corresponding author: Sebastian Geiger, Isotope Geology and Mineral Resources, Department of Earth Sciences, ETH Zürich, Sonneggstr. 5, CH-8092 Zürich, Switzerland, `geiger@erdw.ethz.ch`

[*]Department of Earth Sciences, ETH Zürich, CH-8092 Zürich, Switzerland
[†]Department of Mathematics, Australian National University, Canberra, ACT 0200, Australia
[‡]Department of Earth Science and Engineering, Imperial College London, London SW7 2BP, U.K.
[§]Water Division, ACTEW Corporation, Canberra, ACT 2601, Australia
[¶]Department of Mathematics, ETH Zürich, CH-8092 Zürich, Switzerland

1 Introduction

Modelling the transport of multiphase fluids, for example of water and oil, in the Earth's crust is very challenging. Hydrological properties such as permeability, porosity, and fluid velocity vary over many orders of magnitude. Hydraulic conditions often focus fluid flow in large-scale fluid reservoirs into structures of much smaller scale, for example into fractures. In such cases the scale of interest can vary from the kilometer to the millimeter scale with order of magnitude velocity variations between the different scales (Fig. 1) (Matthäi & Roberts 1996; Matthäi *et al.* 1998; Matthäi & Belayneh 2004). As a further difficulty, constitutive relations for multiphase flow, i.e. the relative permeability and capillary pressure functions, are nonlinear. In certain cases the numerical solution requires computationally costly iterative schemes (Helmig 1997).

Various numerical methods have been applied to model multiphase flow. Traditionally, the governing equations have been solved by finite difference methods (Aziz & Settari 1979). Fully coupled upwind-weighted finite element methods have also found many applications, as they allow for a more realistic representation of geologic structures than finite difference methods (Huyakorn & Pinder 1978; Dalen 1979; Forsyth 1991; Letniowski & Forsyth 1991; Helmig & Huber 1998; Bastian & Helmig 1999). Such methods are mathematically similar to the integrated finite difference method (Narasimhan & Witherspoon 1976), another approach suitable to simulate multiphase flow (Pruess 1991). The key difference between fully coupled upwind-weighted finite element methods and integrated finite difference methods lies in the calculation of the fluid pressure gradient (Narasimhan & Witherspoon 1976). The integrated finite difference method computes the gradient using a finite difference approximation. This requires that the interface between two nodes is perpendicular to the line connecting the nodes. Finite element methods, in general, do not suffer from this restriction because the gradient is calculated on the basis of the element interpolation functions. Therefore, finite element methods commonly allow for a more flexible representation of geological structures, particularly if Delaunay triangulations are used (Shewchuck 2002). Coupled finite element methods, as well as integrated finite difference methods, have the drawback that the resulting algebraic solution matrices are often poorly conditioned and not diagonally dominant. This makes the application of fast matrix solvers difficult. In addition, computationally costly iterative schemes such as Newton's method are needed to solve for the nonlinearities (Huber & Helmig 1999; Burri 2004). Recent advances in the simulation of multiphase flow in complex reservoirs are flux continuous finite difference methods (Lee *et al.* 2002) or hexahedral multi-block methods (Jenny *et al.* 2002).

Combinations of finite element and finite volume methods (FEFVM) are increasingly popular (Eymard *et al.* 1989; Durlofsky 1993; Bergamaschi *et al.* 1998; Huber & Helmig 1999). In this approach, a finite volume subgrid is constructed as a complement to the finite element grid. The geometric flexibility of the finite element method is retained, but in terms of run-time and accuracy, FEFVM simulations yield better results than fully coupled upwind-weighted finite element methods as long as capillary pressures only varies in continuous fashion (Huber & Helmig 1999; Burri 2004). The FEFVM are often embedded within an implicit pressure, explicit saturation formulation (IMPES) to simulate multi-

phase flow in porous media. In the IMPES approach, a parabolic fluid pressure equation (flow equation) is solved implicitly (here using the finite element method) while the saturation field is fixed, yielding the velocities of the fluid phases. These velocities are used to calculate the mass balance of the fluid phases in the hyperbolic continuity (transport) equation (here using the finite volume method) while the pressure field remains fixed (Aziz & Settari 1979).

The IMPES formulation therefore allows the combination of the best features of the finite element and the finite volume method. In particular: The geometric flexibility of the finite-element method allows to resolve the inhomogeneous flow field over several orders of magnitude in scale (Fig. 1). The fluid pressure and continuity equation, which both exhibit nonlinearities, can be decoupled from each other. This avoids the necessity of using a nonlinear solution algorithm such as Newton's method. The fluid pressure equation can be solved efficiently by the finite element method and the transport equation by the finite volume method. When the nonlinear flow and transport equations are decoupled, multigrid solvers are readily applied to solve the system of equations. Algebraic multigrid methods in particular deal well with the large variations in permeability and porosity and solve the symmetric positive definite matrix for the fluid pressure equation (Matthäi & Roberts 1996; Roberts & Matthäi 1996). Mass conservative, second order accurate, total variation diminishing (TVD) finite volume schemes can be used to accurately track the propagation of the saturation fronts when solving the continuity equation.

Here, we will present a finite volume method that is coupled with a standard Galerkin finite element method embedded within an IMPES formulation. A finite volume subgrid is constructed on the basis of the finite element grid. This method is similar to the one discussed in the classical paper of Durlofsky (1993), but it differs in three important points. Durlofsky (1993) uses a mixed finite element solution for the pressure and velocity equations. Because the flux is continuous between two finite elements in this formulation, the finite volumes in the approach by Durlofsky (1993) are equal to the finite elements. Saturation is therefore piecewise constant from element to element. Finally, a higher-order accurate approximation of the flux between two elements (i.e., finite volumes) is obtained by a preprocessing step in which the element saturations are linearly interpolated between three adjacent elements. This gradient is then limited to avoid spurious oscillations.

In the approach presented here, the fluid pressure field is calculated using a standard Galerkin method. The fluid velocity, obtained by element-wise differentiation of the nodal fluid pressure, is constant in each finite element. The finite volume cells are constructed around the corner nodes of each finite element and saturations are calculated at the finite element nodes. The fluid velocities are discontinuous between two adjacent finite elements but continuous between two adjacent finite volumes. Higher-order accurate approximation of the flux between two finite volumes is obtained in a preprocessing step by calculating a linear gradient of the saturations on the basis of a least-squares method using all finite volumes surrounding the one of interest. A limiting procedure is applied as well to avoid spurious oscillations. Our numerical methods are implemented in the object-oriented C++ code CSP (Matthäi *et al.* 2001).

We will demonstrate that the combination of node-centered finite volumes with stan-

dard Galerkin solutions of the pressure equation within the IMPES formulation allows us to efficiently model nonlinear multiphase flow in highly heterogeneous geologic media with complex structures. This method is further fully mass conservative, does not show any grid orientation effects and accurately retains shock fronts and rarefaction fans occurring during multiphase flow.

This paper is structured as follows: In the next section, the governing equations for multiphase flow in geologic media are discussed. This is followed by a detailed description of the discretization, numerical method, and its extension to a second order accurate, TVD scheme for node-centered finite volumes on unstructured grids. Next, the numerical method is compared to an analytical solution, other numerical techniques, and reference solutions. In the last section, we conduct further numerical experiments and apply the FEFVM to hypothetical examples where oil is pumped out of reservoir with a random permeability field and out of a fractured reservoir. We also present an example application of secondary oil migration due to buoyancy driven flow.

2 Governing Equations

Flow of an immiscible fluid phase through porous media is described by the continuity equation and Darcy's law (Bear 1972). Assuming that the fluid and rock matrix are incompressible, the mass balance for a fluid phase α is given by

$$\phi \frac{\partial S_\alpha}{\partial t} = -\nabla \cdot \mathbf{v}_\alpha + q_\alpha \quad \alpha \in \{w, n\} \tag{1}$$

where ϕ is the porosity of the rock and S is the saturation (volume fraction) of phase α. The subscripts w and n denote the wetting (water) and non-wetting (oil) phase, respectively. The saturations S must satisfy the relation $S_w + S_n = 1$. The fluid velocity of phase α is given empirically by Darcy's law:

$$\mathbf{v}_\alpha = -\lambda_\alpha \mathbf{k} \left(\nabla p_\alpha - \rho_\alpha \mathbf{g} \right) \tag{2}$$

The mobility $\lambda_\alpha = k_{r\alpha}/\mu_\alpha$ is the ratio between the relative permeability $k_{r\alpha}$ of phase α and its viscosity μ_α. The relative permeability describes how the presence of a fluid phase perturbs the flow behavior of the other phase and vice versa (Fig. 2). $\mathbf{k}$ is the permeability tensor of the porous medium, p_α is the fluid pressure of phase α, ρ_α is the fluid phase density, and $\mathbf{g} = [0, 0, -g]^T$ is the gravitational acceleration vector. The fluid pressure for the wetting and non-wetting phase are related through the capillary pressure p_c as $p_n = p_w + p_c$. Several classical functions exist for the calculation of relative permeability $k_{r\alpha}$ and capillary pressure p_c (Brooks & Corey 1964; Van Genuchten 1980).

Neglecting capillary effects such that $p_w = p_n$, Darcy's law for both fluid phases can be expressed similarly to equation 2 as

$$\mathbf{v}_t = -\lambda_t \mathbf{k} \nabla p - \mathbf{k}\mathbf{g} \left(\lambda_w \rho_w + \lambda_n \rho_n \right) \tag{3}$$

where $\mathbf{v}_t = \mathbf{v}_w + \mathbf{v}_n$ is the total velocity of the fluid phases and $\lambda_t = \lambda_w + \lambda_n$ is the total mobility.

If the fluid is incompressible, the divergence of the flow field is equal to the total fluid source or sink $q_t = q_w + q_n$

$$\nabla \cdot \mathbf{v}_t = q_t \tag{4}$$

By inserting Darcy's law from equation 3 into equation 4, the following equation for the fluid pressure of incompressible fluids in a reservoir is obtained

$$0 = \nabla \cdot [\lambda_t \mathbf{k} \nabla p] + \mathbf{k} \left(\lambda_w \rho_w + \lambda_n \rho_n\right) g \nabla z + q_t \tag{5}$$

For reservoirs with slightly compressible fluids and/or rock matrix where $c_t(\Delta p) \ll 1$, which is a valid assumption on the reservoir scale (Durlofsky 1993), equation 5 becomes the parabolic fluid pressure equation

$$\phi c_t \frac{\partial p}{\partial t} = \nabla \cdot [\lambda_t \mathbf{k} \nabla p] + \mathbf{k} \left(\lambda_w \rho_w + \lambda_n \rho_n\right) g \nabla z + q_t \tag{6}$$

Here, c_t is the total compressibility of the fluid and rock system.

If we further assume that gravity effects are absent such that for the incompressibility condition the fluid pressure is given by

$$0 = \nabla \cdot [\lambda_t \mathbf{k} \nabla p] \tag{7}$$

then the phase velocity $\mathbf{v}_\alpha$ is equal to

$$\mathbf{v}_\alpha = f_\alpha \mathbf{v}_t \tag{8}$$

where $f_\alpha = \lambda_\alpha / \lambda_t$ is the fractional flow function. This allows rewriting equation 1 as

$$\phi \frac{\partial S_\alpha}{\partial t} = -\nabla \cdot (f_\alpha \mathbf{v}_t) + q_\alpha \tag{9}$$

To include capillary as well as gravity effects, equation 9 must be expanded as (Durlofsky 1993)

$$\phi \frac{\partial S_\alpha}{\partial t} = -\nabla \cdot (f_\alpha \mathbf{v}_t) + \nabla \cdot \left(\bar{\lambda}_t \mathbf{k} \nabla p_c\right) - \nabla \cdot \left(\Delta\rho g \bar{\lambda}_t \mathbf{k} \nabla z\right) + q_\alpha \tag{10}$$

where $\bar{\lambda}_t$ is defined as $\bar{\lambda}_t = \left(\lambda_n \lambda_w\right) / \lambda_t$ and $\Delta\rho$ as $\Delta\rho = \rho_\alpha - \rho_{\alpha 2}$, the subscript 2 denoting the second phase. Note that the capillary pressure term has a positive sign if $\alpha = n$ and negative sign if $\alpha = w$. For capillary pressure, the transient fluid pressure equation (Eq. 6) becomes (Durlofsky 1993)

$$\phi c_t \frac{\partial p}{\partial t} = \nabla \cdot [\lambda_t \mathbf{k} \nabla p] + \nabla \cdot \left[\frac{1}{2} \left(\lambda_n - \lambda_w\right) \mathbf{k} \nabla p_c\right] + \mathbf{k} \left(\lambda_w \rho_w + \lambda_n \rho_n\right) g \nabla z + q_t \tag{11}$$

3 Numerical Methods

3.1 Choice of Discretization

In order to capture the flow geometry with the flexibility that the finite element method offers, we discretize the two-dimensional domain with a constrained conforming Delaunay triangulation (Shewchuck 2002), see Figure 3. The finite volumes are constructed from the basis of the finite elements. A common choice for triangular finite element grids is to use node-centered finite volumes (Durlofsky 1994; Huber & Helmig 2000). For a given triangular finite element mesh, a finite volume subgrid is constructed by connecting the barycenters of the triangles with the midpoints of the associated edges (Fig. 4).

3.2 Calculation of Fluid Velocities

In the IMPES formulation, an accurate representation of the fluid velocity field is essential for calculating the advance of the fluid phases. The best technique to calculate fluid velocities from the fluid pressure field using finite element methods has been subject of considerable discussion (Cordes & Kinzelbach 1992; Durlofsky 1994; Mosé *et al.* 1994; Cordes & Kinzelbach 1996). In general, two approaches based on different finite element formulations are possible. The first one is a mixed-element formulation in which fluid pressures are calculated at the element centers and fluid fluxes are obtained simultaneously at the midpoints of the finite element edges (Chavent & Jaffre 1986). The flux calculated by the mixed-element method is continuous across adjacent finite elements. This approach is commonly used in the IMPES formulation (Eymard *et al.* 1989; Durlofsky 1993; Bergamaschi *et al.* 1998; Huber & Helmig 1999). The second approach is to calculate the fluid velocities by element-wise differentiation of the pressure field. This has been successfully employed in high-resolution simulations of fluid flow in complexly fractured networks and porous media using linear (Matthäi & Roberts 1996; Matthäi *et al.* 1998) and quadratic (Matthäi & Belayneh 2004) finite element interpolation functions. For linear interpolation functions, the velocities are element-wise constant and hence discontinuous between two adjacent elements. They are, however, continuous between adjacent node-centered finite volumes (Fig. 5). By integrating the flux at each segment, i.e. the product of velocity, normal vector, and segment length, over the entire surface of the finite volume, conservation of mass is obtained on the finite volumes (Durlofsky 1994).

Either method has distinct advantages and disadvantages. It has been argued that the continuous fluxes of the mixed-element formulation commonly yield more accurate streamlines, particularly for coarse meshes and strongly heterogeneous permeability fields (Durlofsky 1994; Mosé *et al.* 1994). On the other hand, mixed-element methods produce solution matrices that are no longer symmetric positive definite and contain between 1.5 to 4 times more unknowns as in standard finite element methods (Durlofsky 1994; Cordes & Kinzelbach 1996). It further can be shown that the lowest order mixed-element methods yields the same results (pressure, velocity, and flux) as linear triangular finite elements (Cordes & Kinzelbach 1996). Cordes & Kinzelbach (1992) use a postprocessing technique

to increase the accuracy of element-wise differentiated velocities. The error of the velocity field computed from mixed-element or Galerkin methods is approximately the same for sufficiently large models (Lachassagne *et al.* 1989) because mixed-element methods approximate the conductivity in the stiffness matrix as the harmonic mean while standard Galerkin methods approximate it by arithmetic weighting (Cordes & Kinzelbach 1996). Mixed-element methods therefore underestimate the total flux while standard Galerkin methods overestimate it. Hydrological scenarios are hence likely to occur where either method is closer to the true solution (Cordes & Kinzelbach 1996). Due to the successful applications of Galerkin methods to model fluid flow in strongly heterogeneous porous and fractured media (Matthäi & Roberts 1996; Matthäi *et al.* 1998; Matthäi & Belayneh 2004) and its suitability for applications of fast matrix solvers such as algebraic multigrid methods (Roberts & Matthäi 1996), we employ the Galerkin finite element method to calculate the fluid pressure field and use element-wise differentiation for the fluid velocities. This method is described in the next section.

3.3 Finite Element Method

We use a standard Galerkin finite element method, where the transport parameters (i.e., $\mathbf{k}, \phi, q$) are defined on the finite elements, to approximate the spatial operators in equation 6. If capillary pressure is present, then we approximate equation 11 and solve for the wetting phase pressure p_w. For simplicity, we first explain the finite element approximation of equation 6 and expand this later to include capillary pressure (Eq. 11). The backward Euler method is used to discretize the time derivative. This yields the fluid pressure at the nodes of the finite elements at each time step. The nodal fluid pressure is differentiated to compute the total velocities from Darcy's law (Eq. 3). Fluid flux conserves mass across the boundary segments of finite volumes within associated finite elements (Fig. 5).

The Galerkin finite element method is well established and excellent descriptions are available in the literature (Huyakorn & Pinder 1983; Zienkiewicz & Taylor 2000). Therefore, only a brief description is provided here.

The computational domain Ω is discretized into a family of triangular finite elements (Fig. 3). We also consider a finite element space $\mathcal{V}$ of linear polynomial functions which are restricted to each triangle in the finite element mesh. For each such finite element space there is a set of m Lagrange points $\mathcal{N}_h = \{\mathbf{x}_i\}_{i=1}^m$ and a set of basis functions $\{\Phi_i\}_{i=1}^m \subset \mathcal{V}$ such that

$$\Phi_i(\mathbf{x}_j) = \begin{cases} 1 & \text{if } i = j, \\ 0 & \text{otherwise.} \end{cases} \tag{12}$$

$\mathbf{x}_j$ is the coordinate vector at node j. Any $v \in \mathcal{V}$ can be written as

$$v(\mathbf{x}) = \sum_{j=1}^{M} v(\mathbf{x}_j)\Phi_j(\mathbf{x}). \tag{13}$$

Consider a general differential equation

$$L[u] = 0 \tag{14}$$

where L is a spatial differential operator. The Galerkin finite element approximation to the solution of this equation is obtained as the function $u \in \mathcal{V}$ which satisfies

$$\int_\Omega L[u]\ \Phi_i\ d\mathbf{x} = 0 \tag{15}$$

for all basis functions Φ_i. This leads to a set of m (possibly nonlinear) equations which need to be solved for the coordinates of u in the given basis $\{\Phi_i\}_{i=1}^m$.

The Galerkin finite element form of equation 6 is given by a function $p(x,t)$ such that for fixed time t, the function $p(\cdot,t) \in \mathcal{V}$. The function p satisfies

$$\begin{aligned}\int_\Omega \phi c_t \frac{\partial p}{\partial t}\Phi_i\ d\mathbf{x} \quad &= \quad -\int_\Omega \lambda_t \nabla p \mathbf{k} \nabla \Phi_i\ d\mathbf{x} \\ &\quad -\int_\Omega \left(\lambda_n \rho_n + \lambda_w \rho_w\right) \mathbf{g}^T \mathbf{k} \nabla \Phi_i\ d\mathbf{x} + \int_\Omega q_t \Phi_i\ d\mathbf{x}\end{aligned} \tag{16}$$

for all basis functions Φ_i. p is represented by the interpolation function

$$p(\mathbf{x},t) = \sum_{j=1}^m p_j(t)\Phi_j(\mathbf{x}) \tag{17}$$

In terms of the functions $p_j(t) = p(\mathbf{x}_j,t)$, equation 16 can be written as the coupled system of algebraic differential equations

$$\sum_{j=1}^m \frac{dp_j}{dt}(t)A_{ij}(t) = -\sum_{j=1}^m p_j(t)K_{ij}(t) + q_i(t). \tag{18}$$

where

$$A_{ij}(t) = \int_\Omega \phi c_t \Phi_j \Phi_i\ d\mathbf{x} \quad \text{and} \quad K_{ij}(t) = \int_\Omega \lambda_t \nabla \Phi_j \mathbf{k} \nabla \Phi_i\ d\mathbf{x} \tag{19}$$

and

$$q_i(t) = -\int_\Omega \left(\lambda_n \rho_n + \lambda_w \rho_w\right) \mathbf{g}^T \mathbf{k} \nabla \Phi_i d\mathbf{x} + \int_\Omega q_t \Phi_i\ d\mathbf{x} \tag{20}$$

Using backward Euler time-stepping to solve this system of equations, we obtain an equation for p_j^k where the superscript k denotes the approximation of the function at time $k\Delta t$, where Δt is the time-step. The evolution equation for p_j^k is given by

$$\sum_{j=1}^m (A_{ij}^{k+1} + \Delta t K_{ij}^{k+1})p_j^{k+1} = \sum_{j=1}^m A_{ij}^k p_j^k + \Delta t q_i^{k+1} \tag{21}$$

Mass lumping, i.e. diagonalization, of the matrix A_{ij} is common and was shown to be essential to avoid spurious oscillations for simulations of unsaturated flow (Celia *et al.* 1990). Each finite element mass matrix is diagonalized by summing up all entries of a row

$$\tilde{A}_{e,ij} = \begin{cases} \sum_{j=1} A_{e,ij} & \text{for } i = j \\ 0 & \text{for } i \neq j \end{cases} \tag{22}$$

Capillary pressure effects are included by the finite element discretization of the term $\nabla \frac{1}{2} \left[(\lambda_n - \lambda_w) \, \mathbf{k} \nabla p_c \right]$ in equation 6 and its addition to the right-hand side $q_i(t)$ in equation 20 as

$$\frac{1}{2} \int_\Omega (\lambda_n - \lambda_w) \, \nabla p_c^T \mathbf{k} \nabla \Phi_i d\mathbf{x} \tag{23}$$

Equation 21, which may be written as $A\mathbf{x} = \mathbf{b}$, is sparse, symmetric, and positive definite and can be solved efficiently using (algebraic) multigrid methods (Roberts & Matthäi 1996; Stüben 2001). A multigrid solver repeatedly applies a v-cycle, during which $\mathbf{x}$ is approximated by the trial solution $\tilde{\mathbf{x}}$. This solution is then smoothed and the grid is coarsened, i.e. the problem $A\mathbf{x} = \mathbf{b}$ is restricted recursively to smaller grids until the problem can be solved exactly on the coarsest grid, for example by LU decomposition. This solution is then interpolated back onto successively finer grids until an improved trial solution $\tilde{\mathbf{x}}$ is obtained. Repeated smoothing, grid coarsening, and interpolation will then lead to a trial solution that solves the problem $A\mathbf{x} = \mathbf{b}$ within numerical precision. In particular, algebraic multigrid solvers do not require any geometric information of the domain and can therefore be used as a plug-in that yields the most efficient method to solve problems with very large numbers of unknowns in geometrically complex structures (Stüben 2001).

We obtain the element-wise constant phase velocity $\mathbf{v}_\alpha$ in a post-processing step after solving equation 21 from

$$\mathbf{v}_{\alpha j} = \sum_{i,j}^{n,d} -p_{\alpha i} \mathbf{k}_{ij} \nabla \Phi_{ji} \lambda_\alpha + \mathbf{k}_{ij} \lambda_\alpha \mathbf{g}_j \rho_\alpha \tag{24}$$

Here, i and j are indices over the n nodes of e, respectively its dimension d. $\nabla\Phi$ is a matrix of size $d \times n$ holding the derivatives of Φ. λ_α and ρ_α are assumed, for simplicity, to be constant in e.

3.4 Finite Volume Method

In the finite volume method, the element-wise constant velocities calculated from equation 24 are employed to compute the mass balance for the fluid phases (Eq. 1). For simplicity, we first assume that capillary and gravity effects are absent and derive the complete finite volume formulation including capillary and gravitational flow later. We use the identity $\mathbf{v}_\alpha = f_\alpha \mathbf{v}_t$ and integrate equation 9 over a finite volume V_i

$$\int_{V_i} \phi \frac{\partial S_\alpha}{\partial t} \, dV = - \int_{V_i} \nabla \cdot (f_\alpha \mathbf{v}_t) \, dV + \int_{V_i} q_\alpha \, dV \tag{25}$$

Within each finite volume V_i, the saturation S_α is assumed to be constant. Applying the divergence theorem to equation 25 leads to the accumulation of all segment fluxes in and out of V_i

$$\int_{V_i} \phi_i \frac{\partial S_\alpha}{\partial t} \, dV = -\frac{1}{A_i} \sum_j^{n_{si}} \left[f_{\alpha j} \mathbf{v}_{tj} \right]^k \cdot \mathbf{n}_j + \frac{\Delta t}{A_i} \sum_e^{n_{ei}} \frac{1}{3} q_{\alpha e}^k A_e \tag{26}$$

where $\sum_j^{n_{si}}$ is the summation of all fluxes $[f_{\alpha j}\mathbf{v}_{tj}]\cdot\mathbf{n}_j$ at segment j belonging to the group of segments n_{si} of finite volume V_i. A_i is the area of the control volume, A_e that of the finite element, and $\mathbf{n}_j$ is the outward normal vector to j-th segment, scaled by the length of the segment. As the source/sink terms q_α are defined on the finite elements, their contribution to a finite volume i is computed by summation $\sum_e^{n_{ei}}$ of each source term associated with a finite element e that belongs to the group of finite elements n_{ei} connected to the finite volume V_i. Note that source/sink terms must be multiplied by 1/3 because each finite element contributes 1/3 of its volume to the associated finite volumes (Fig. 4). Using a forward Euler discretization in time on equation 26 yields, after rearranging, the evolution of S_α in V_i from time k to $k+1$ in the final form

$$S_{\alpha i}^{k+1} = S_{\alpha i}^{k} - \frac{\Delta t}{\phi_i A_i}\sum_j^{n_{si}}[f_{\alpha j}\mathbf{v}_{tj}]\cdot\mathbf{n}_j + \frac{\Delta t}{\phi_i A_i}\sum_e^{n_{ei}}\frac{1}{3}q_{\alpha e}A_e \tag{27}$$

where Δt is the time-step. Its size is given by the CFL criterion, stating that the maximum volume flux per time-step must not exceed the area of the associated finite volume.

If capillary and gravity effects are present, equation 25 must include the divergence terms for capillary pressure and gravity from equation 10

$$\begin{aligned}\int_{V_i}\phi\frac{\partial S_\alpha}{\partial t}\,dV = &- \int_{V_i}\nabla\cdot(f_\alpha\mathbf{v}_t)\,dV \\ &+ \int_{V_i}\nabla\cdot\left(\bar{\lambda}_t\mathbf{k}p_c\right)\,dV \\ &- \int_{V_i}\nabla\cdot\left(\Delta\rho g\bar{\lambda}_t\mathbf{k}\nabla z\right)\,dV + \int_{V_i}q_\alpha\,dV\end{aligned} \tag{28}$$

Applying the same procedure to equation 28, i.e. the divergence theorem and forward Euler discretization in time, yields the finite volume formulation including the segment fluxes for capillary and gravity flow

$$\begin{aligned}S_{\alpha i}^{k+1} = S_{\alpha i}^{k} &- \frac{\Delta t}{\phi_i A_i}\sum_j^{n_{si}}[f_{\alpha j}\mathbf{v}_{tj}]^k\cdot\mathbf{n}_j \\ &+ \frac{\Delta t}{\phi_i A_i}\sum_j^{n_{si}}\left[\bar{\lambda}_{tj}\nabla p_c\right]^k\cdot\mathbf{n}_j \\ &- \frac{\Delta t}{\phi_i A_i}\sum_j^{n_{si}}\left[\Delta\rho g\bar{\lambda}_{tj}\mathbf{k}\nabla z\right]^k\cdot\mathbf{n}_j + \frac{\Delta t}{\phi_i A_i}\sum_e^{n_{ei}}\frac{1}{3}q_{\alpha e}^k A_e\end{aligned} \tag{29}$$

Note that ∇p_c and $\Delta\rho$ are, as $\mathbf{v}_\alpha$, element-wise constant.

3.4.1 Second-order Accuracy and Slope Limiters

A first-order accurate scheme for solving equation 27 or 29 is obtained if we approximate $S_{\alpha i}$ by a constant for each volume V_i and compute the flux at segment j using a simple

upwinding scheme, i.e. calculating $f_{\alpha j}$ and $\bar{\lambda}_{tj}$ from $S_{\alpha i}$ at the finite volume V_i^{up} that lies upstream of j. This leads to highly diffuse non-physical saturation fronts. A higher-order accurate approximation of $S_{\alpha i}$, respectively $f_{\alpha j}$ and $\bar{\lambda}_{tj}$, is hence needed.

We obtain a second-order accurate solution of equation 27 or 29 by reconstructing the linear gradient of the saturation $S_{\alpha i}$ in the control volume V_i. This is achieved by using a least squares method to fit a plane through $S_{\alpha i}$ and the saturation values $S_{\alpha j}$ at the n_i neighboring control volumes V_j of V_i, such that $S_{\alpha i}$ varies linearly in V_i. In two dimensions, this gradient $\mathbf{a} = (a_1, a_2)$ satisfies

$$\sum_{l=1}^{2} M_{kl} a_l = b_k \tag{30}$$

where

$$M_{kl} = \sum_{j=1}^{n} (x_{jk} - x_{ik})(x_{jl} - x_{il}) \tag{31}$$

and

$$b_k = \sum_{j=1}^{n} (S_{wj} - S_{wi})(x_{jk} - x_{ik}) \tag{32}$$

and x_{i1} and x_{i2} are the two-dimensional spatial coordinates of the center of mass of finite volume V_i, and x_{j1} and x_{j2} are the spatial coordinates of the center of mass of the neighboring finite volumes V_j. The linearly approximated saturation $\tilde{S}_{\alpha j}$ is, at any point within the finite volume V_i, is given by

$$\tilde{S}_{\alpha i}(\mathbf{x}) = S_{\alpha i} + \mathbf{a} \cdot (\mathbf{x} - \mathbf{x}_i) \tag{33}$$

where $\mathbf{x} \in V_i$. Evaluating $\tilde{S}_{\alpha i}$ at each segment j, the fractional flow $f_{\alpha j}$ is then calculated for $\tilde{S}_{\alpha i}$ at the upstream finite volume V_i^{up} such that equation 27 or 29 is solved to second-order accuracy.

Although second-order accuracy in space is now achieved, the linear reconstruction $\tilde{S}_{\alpha i}$ will introduce spurious oscillations resulting in non-physical values of S_α, because $f_{\alpha j}$ may over- or under-predict the flux where sudden jumps (shocks) in S_α occur over two adjacent finite volumes. The application of a slope limiter is hence essential to smooth the gradient of $S_{\alpha i}$ if such shock fronts occur. In particular the limited function $\bar{S}_{\alpha i}$ is obtained for $\tilde{S}_{\alpha i}$ as

$$\bar{S}_{\alpha i}(\mathbf{x}) = S_{\alpha i} + \Psi_i \left(\mathbf{a} \cdot (\mathbf{x} - \mathbf{x}_i)\right) \tag{34}$$

where $0 \leq \Psi_i \leq 1$ is a chosen limiter. With $\Psi_i = 1$, the gradient of $S_{\alpha i}$ is fully retained. With $\Psi_i = 0$, the saturation $S_{\alpha i}$ is constant in V_i resulting in a first-order scheme. With $0 < \Psi_i < 1$, the gradient of $S_{\alpha i}$ is limited by a factor Ψ_i. Values of $\Psi_i < 1$ occur in the vicinity of shock fronts (i.e., discontinuous changes of S_α) to limit the gradient and avoid spurious oscillations.

We use the MINMOD limiter to calculate Ψ_j as the minimum of a value r_i or 1

$$\Psi_j = \min\left[r_i, 1\right] \tag{35}$$

The minimum of r_i is calculated by comparing S_α at finite volume i and its linear approximation $\tilde{S}_{\alpha j}$ at all segments j belonging to i

$$r_i = \begin{cases} (S_{\alpha i}^{\max} - S_{\alpha i})/(\tilde{S}_{\alpha j} - S_{\alpha i}) & \tilde{S}_{\alpha j} > S_{\alpha i} \\ (S_{\alpha i}^{\min} - S_{\alpha i})/(\tilde{S}_{\alpha j} - S_{\alpha i}) & \tilde{S}_{\alpha j} < S_{\alpha i} \\ 1 & \tilde{S}_{\alpha j} = S_{\alpha i} \end{cases}$$

$S_{\alpha i}^{\min}$ and $S_{\alpha i}^{\max}$ is the minimum, respectively maximum value of S_α at finite volume i and $\tilde{S}_{\alpha j}$ at all its segments j. Solving equation 29 with $f_{\alpha j}$ and $\bar{\lambda}_{tj}$ calculated for the linearly approximated and limited saturation $\bar{S}_{\alpha j}$ at segment j of the upstream finite volume V_i^{up} yields

$$\begin{aligned} S_{\alpha i}^{k+1} = S_{\alpha i}^{k} \quad & - \quad \frac{\Delta t}{\phi_i A_i} \sum_j^{n_{si}} \left[f_{\alpha j} \left(\bar{S}_{\alpha j} \right) \mathbf{v}_{tj} \right]^k \cdot \mathbf{n}_j \\ & + \quad \frac{\Delta t}{\phi_i A_i} \sum_j^{n_{si}} \left[\bar{\lambda}_{tj} \left(\bar{S}_{\alpha j} \right) \nabla p_c \right]^k \cdot \mathbf{n}_j \\ & - \quad \frac{\Delta t}{\phi_i A_i} \sum_j^{n_{si}} \left[\Delta \rho g \bar{\lambda}_{tj} \left(\bar{S}_{\alpha j} \right) \mathbf{k} \nabla z \right]^k \cdot \mathbf{n}_j + \frac{\Delta t}{\phi A_i} \sum_e^{n_{ei}} \frac{1}{3} q_{\alpha e}^k A_e \end{aligned} \tag{36}$$

Such total variation diminishing (TVD) schemes (Harten 1983; Sweby 1984) appear to be computationally the most efficient methods when applied to a simple one-dimensional, linear conservation law such as the advection equation. Therefore, TVD methods are usually employed to solve the advection equation within the FEFVM framework (Eymard *et al.* 1989; Durlofsky 1993; Bergamaschi *et al.* 1998; Huber & Helmig 1999).

4 Validation of the Numerical Methods

4.1 Buckley-Leverett Problem

If gravity and capillary effects are neglected, the multiphase flow problem reduces to the Buckley-Leverett problem (Buckley & Leverett 1942), for which analytical solutions can be derived (Helmig 1997). Our numerical method is compared to an analytical solution of the one dimensional Buckley-Leverett problem using the relative permeability functions

$$k_{rw}(S_w) = S_w^4$$

and

$$k_{rn}(S_w) = (1 - S_w)^2(1 - S_w^2)$$

of the Brooks-Corey model (Brooks & Corey 1964) with a pore size distribution index of 2 (Fig. 2). We chose a uniform isotropic permeability of $\mathbf{k} = 10^{-13}$ m^2, a uniform porosity $\phi = 0.15$ and a fluid pressure gradient of 1000 Pa m^{-1}. The viscosity of the water phase

μ_w and the oil phase μ_n are the same at 0.001 Pa s^{-1}. Initially, the medium is saturated with oil ($S_n = 0.9$) that is replaced from the left by the intruding water phase with a saturation of $S_w = 0.9$. The meshes are pseudo one-dimensional with uniform triangular finite elements and consist of 60 and 200 nodes, respectively, in the x-direction. The fluid pressure is updated every 0.1 days.

Figure 6 shows the comparison of the numerical solution for the coarse and fine meshes with the analytical solution for the Buckley-Leverett problem after 105 days. The numerical solution shows a very good agreement with the analytical solution. Numerical diffusion at the shock front is minimal and the rarefaction fan, i.e. the nonlinear change in S_w to the left of the shock front, is matched very closely. The solution improves as the mesh is refined.

4.2 Comparison to other Methods

We now present a comparison of the numerical results for the Buckley-Leverett problem to results obtained with an upwind-weighted, fully coupled finite element method (Huyakorn & Pinder 1978; Dalen 1979; Forsyth 1991; Helmig & Huber 1998) implemented into CSP by Burri (2004) and with the integrated finite difference method (Narasimhan & Witherspoon 1976) using TOUGH (Pruess 1991). The same parameters as in the FEFVM simulations were used for the fully coupled finite element and TOUGH simulations. Furthermore, simulations carried out with TOUGH used an upstream weighting of mobility and permeability. The module EOS8 was employed with the appropriate adjustment of the relative permeability model for the oil phase. The oil viscosity was fixed at 0.001 Pa s^{-1}. The gas phase was absent. The temperature was held uniform at 20°C and pressures varied from 1.1×10^6 Pa at the left boundary to 1.0×10^5 Pa at the right boundary such that the water viscosity was constant at 0.001 Pa s^{-1} in the entire model while retaining a pressure gradient of 1000 Pa m^{-1}.

Figure 7 shows the results for the coarse mesh (60 nodes in x-direction) after 105 days. Clearly, the FEFVM matches the analytical solution the closest. The fully coupled finite element solution is also in relatively good agreement with the analytical solution but does not match the shock front as well. The results obtained with TOUGH show the strongest deviation from the analytical solution. The location of the shock front agrees partly but the resolution of shock front is very diffuse. The numerical solutions with TOUGH improve significantly as the mesh is refined. For the fine mesh (200 nodes in x-direction, not shown), the numerical solution matches that of the fully coupled finite element method for the coarse mesh. The fully coupled finite element method, however, has the drawback that it requires significantly more CPU time due to the use of iterative schemes (Table 1).

4.3 Five-spot Waterflood Problem

In order to test the sensitivity of our numerical scheme to grid orientation effects we apply it to the five-point waterflood problem (Spivak *et al.* 1977). This problem consists of two test cases, neglects capillary and gravity effects, and only considers incompressible

and immiscible fluid flow. In both cases, a square domain (here 100×100 meters with $\mathbf{k} = 10^{-14}$ m^2) is initially saturated with oil ($S_n = 1.0$). In the first case (Fig. 8a), water is injected in the lower left corner ($S_w = 1.0$), replacing the oil, which is extracted in the upper right corner. Here, the principal flow direction is diagonal to the grid. In the second case (Fig. 8b), water is injected in the lower left and upper right corners ($S_w = 1.0$), oil is replaced and extracted in the lower right and upper left corners, respectively. Here, the flow is parallel to the grid. In both cases, the pumping rates are held constant. We solve the five-point waterflood problem for finite element grids consisting of 4,096 and 32,768 triangular finite elements using the same Brooks-Corey function and viscosity ratio as for the Buckley-Leverett test case. The fluid pressure field is updated every 4.32×10^{-4} pore volumes injected (PVI).

Figure 9 shows the saturation contours for the water phase for both cases after 0.015 PVI. A good numerical scheme should reproduce quarter circle shaped saturation fronts or the water phase (Spivak *et al.* 1977). For the coarse and the fine mesh, the numerical scheme does not show major grid orientation effects or cross diffusion and the saturation fronts are represented by highly resolved quarter circles.

5 Two-phase Flow in Heterogeneous Reservoirs

In the following, three numerical experiments are discussed which test the applicability of our method to simulations of multiphase flow in highly-heterogeneous reservoirs represented by regular and irregular triangulated finite element meshes. The first test case considers flow in a porous medium with a random permeability field, the second test case describes flow towards a pumping well within an idealized fractured reservoir. The same relative permeability model as in section 4 is used. The last test-case comprises buoyancy driven hydrocarbon migration in an idealized faulted sedimentary basin.

5.1 Flow in a Random Permeability Field

We have modeled flow in a square domain with a random permeability structure. The model setup is analogous to the first test case of the five-spot waterflood problem (Fig. 8a). Water is injected in the lower left corner at a constant rate ($S_w = 1.0$) into a reservoir initially fully saturated with oil ($S_n = 1.0$). Oil is pumped out of the reservoir in the upper right corner. In both cases, pumping rates are held constant. A random permeability field was created using a log normal distribution, a mean of -12.0, a variance of 0.3, and a correlation length of 2.0 (Bellin & Rubin 1996). The fine triangular finite element discretization of the five-spot waterflood problem consisting of 32,768 elements was used.

Figure 10 shows the permeability field and the numerical solution of the water phase after 0.015 PVI. Our method retains the shock fronts even in a permeable medium with permeability variations over four orders of magnitude.

5.2 Flow Towards a Pumping Well Within an Interconnected Fracture Model

Faults in oil reservoirs have a strong influence on the total permeability and cause difficulties when predicting oil recovery (Matthäi & Roberts 1996; Matthäi *et al.* 1998) (Fig. 1). Furthermore, permeability fields are discontinuous because variations in permeability are bound to distinct geological structures. To study the ability of the numerical method to model pumping in a reservoir with an idealized interconnected fracture system, flow around a well located in the center of an interconnected fracture network is examined (Fig. 11). All fractures have an equivalent porous media representation and are represented as thin cuts (10 cm) in a plan view of the reservoir. The fracture aperture is still over-represented by a factor 100 and the effective medium permeability has been adjusted accordingly. The matrix permeability in the reservoir is set to $\mathbf{k}_m = 10^{-13}$ m^2 while the fracture permeability is $\mathbf{k}_f = 10^{-9}$ m^2. The matrix porosity is $\phi_m = 0.1$ while the fracture porosity is $\phi_f = 1.0$. The oil phase is twice as viscous as the water phase. Initially, the reservoir is assumed to be completely filled with oil ($S_n = 1.0$) and subsequently pumped empty (Dirichlet conditions of $S_w = 1.0$ along the boundaries of the model). Reservoir boundary pressures are fixed, simulating infinite-acting reservoir behavior. The model dimensions are 50×50 meters. The unstructured mesh consisted of 20,586 finite elements. Element areas vary from 0.001 to 1 m^2. The smallest triangles are located within the fractures. The fluid pressure is updated every 0.025 pore volumes extracted (PVE).

Figure 12 shows that the presence of conductive fractured leads to dramatic deviations from radial drawdown. Water is focused into the fractures where the flow is fastest. Oil can be extracted efficiently through the fractures but only slowly from some parts of the matrix. The oil within the fracture-bounded block in the reservoir around the well (i.e., the part of the reservoir that is totally surrounded by fractures) is recovered first and displaced by water. This implies that oil-production rate rapidly decreases with time as water break through in the well occurs long before any of the oil in most parts of the matrix has been mobilized.

5.3 Secondary Migration in a Faulted Reservoir

To illustrate the ability of the numerical method to compute density driven two-phase flow on the reservoir scale, we have modeled two-phase flow including gravity and capillary effects to simulate secondary migration within an idealized faulted sedimentary basin. The sedimentary basin comprises an anticlinal structure that is offset by two normal faults that are highly permeable. The anticline consists of four different sedimentary layers. Its top layer (Layer 4) has the low permeability of 10^{-16} m^2 and high capillary entry pressure of 10000 Pa. It hence forms a barrier. Table 2 lists the properties of the different sedimentary layers. We assume that oil is lighter than water, having a density of $\rho_n = 800$ kg m^{-3} while the water phase has a density of $\rho_w = 1000$ kg m^{-3}. Furthermore, oil is assumed to be three times as viscous as water. Dirichlet boundary conditions were applied at the top and bottom model boundary for the oil saturations and on the top boundary for the fluid

pressure. The oil source is initially entirely saturated with oil ($S_n = 0.9$), the overlying reservoir entirely with water ($S_w = 1.0$).

Figure 14 shows the oil movement after 2000 and 4000 years of migration, respectively. In this hypothetical example, oil rises in a series of individual fingers from its source region. Water is being displaced by the buoyant oil and sinks down. In the shallower part of the model, oil is trapped below the low-permeability layer of the anticline. Since oil is lighter than water, it flows underneath this barrier to the top of the anticline. As oil accumulates below the low-permeability layer, the capillary pressure increases. When the capillary pressure in the layer below the barrier is higher than the barrier's entry pressure, small amounts of oil diffuse into the low-permeability layer due to the capillary pressure gradient (Fig. 14b). Where the fault zone breaks the barrier, oil rapidly discharges into the sediments above. It is interesting to note that the flow is not distinctly focused into the high-permeability faults. Oil only flows through the fault zone where the fault cross-cuts the low-permeability layer.

6 Discussion

The presented combination of a node-centered finite volume method with a standard Galerkin finite element method is well suited to model multiphase flow in structurally complex geologic media. It is computationally more efficient and accurate than alternative fully coupled solution techniques using finite element or integrated finite difference discretizations. The technique is an interesting alternative to the approach discussed by Durlofsky (1993), because it does not need a mixed-element formalism. It hence can be implemented straightforwardly into existing finite element (or finite difference) codes that can solve parabolic and elliptic partial differential equations.

Three limitations of the combined finite element-finite volume method, however, exist. First, the storage and CPU requirements necessary to construct a 3D finite volume subgrid from tetrahedral elements are high. This makes the method less efficient for 3D simulations. The number of finite elements, and consequently finite volumes, can be reduced significantly if mixed finite element meshes are used in three dimensions (Matthäi 2003).

Second, if extremely high fluid velocities occur in very small finite volumes, the explicit solution of the continuity equation requires very small time-steps, which increases the CPU time. A possibility to circumvent this problem could be the use of finite volume time domain methods. These techniques are commonly employed in numerical simulations of electromagnetic processes (Fumeaux *et al.* 2004). They partition the finite volume domain into several sub-domains where local time-steps can be applied without violating the stability criterion.

Last, Huber & Helmig (1999) have discussed that a finite volume discretization of the capillary flux (Eq. 29) leads to instabilities in the numerical solution if the capillary pressure varies discontinuously at material interfaces. It is, however, possible to derive an alternative, numerically more stable formulation for the capillary pressure (Helmig 1997).

Using the chain rule, ∇p_c can be expressed as

$$\nabla p_c = \frac{dp_c}{dS_\alpha} \nabla S_\alpha \tag{37}$$

Note that dp_c/dS_α has a positive sign if $\alpha = n$ and negative sign if $\alpha = w$. By inserting this identity into the capillary pressure term of equation 10, the following nonlinear diffusion equation can be derived

$$\phi \frac{\partial S_\alpha}{\partial t}_{\text{diff}} = \nabla \cdot \left(\bar{\lambda}_t \mathbf{k} \frac{dp_c}{dS_\alpha} \nabla S_\alpha \right) \tag{38}$$

This equation describes the diffusive spreading of the saturation due to capillary pressure effects with the diffusivity given by the term $\bar{\lambda}_t \mathbf{k} dp_c/dS_\alpha$. Due to its parabolic nature, it is well suited for solution by implicit finite element methods. Its solution can occur before or after the finite volume calculation of the advective transport of the fluid phases. While this formulation is numerically more stable than the finite volume discretization of the ∇p_c term (Eq. 29) it under-predicts, however, the possible build-up of saturation at material interfaces (Helmig 1997; Burri 2004).

7 Conclusions

We have combined a standard Galerkin finite element method with a second order accurate TVD finite volume method to model multiphase fluid flow in the Earth's crust. This technique applies an implicit pressure, explicit saturation formalism. The use of least-squares methods to obtain a TVD method for node-centered finite volumes allows us to compute very precise numerical solutions that accurately preserve shock fronts and rarefaction fans. Cross-diffusion is virtually absent in this TVD scheme. This approach proves as an efficient way to model two-phase flow of incompressible fluids in geologic media with complex geometrical structures and large variations and discontinuous changes in the hydrological rock properties (permeability, porosity) and fluid velocities. Our node-centered finite volume method does not require the use of a mixed-element formulation to solve for fluid pressure and fluid velocity simultaneously.

8 Acknowledgments

We thank Patrick Jenny and Dim Coumou for thoughtful comments and helpful discussions, Ivan Lunati for his help with the TOUGH simulations, and Mark Person and an anonymous reviewer for their constructive criticism, which has improved this manuscript. Funding was provided by the Swiss National Science Foundation, grants SNF-20-59544.99 and 20002-100735/1.

References

Aziz K and Settari A (1979) *Petroleum Reservoir Simulation*, Applied Science Publishers, London.

Bastian P and Helmig R (1999) Efficient fully-coupled solution techniques for two-phase flow in porous media. Parallel multigrid solution and large scale computations. *Advances in Water Resources*, **23**, 199–216.

Bear J (1972) *Dynamics of Fluids in Porous Media*, Dover, New York.

Bellin A and Rubin Y (1996) Hydrogen: A spatially distributed random field generator for correlated properties. *Stochastic Hydrology and Hydraulics*, **10**, 253–278.

Bergamaschi L, Mantica S and Manzini G (1998) A mixed finite element-finite volume formulation of the black-oil model, *SIAM Journal on Scientific Computing*, **20**, 970–997.

Brooks RH and Corey AT (1964) *Hydraulic properties of porous media.* Hydrological Paper 3, Colorado State University.

Buckley SE and Leverett MC (1942) Mechanisms of fluid displacement in sands, *Transactions of the American Institute of Mining and Metallurgical Engineers AIME*, **146**, 107–116.

Burri A (2004), *Implementation of a Multiphase Flow Simulator using a Fully Upwind Galerkin Method within the CSP Multiphysics Toolkit*. Unpublished Diploma Thesis ETH Eidgenössische Technische Hochschule Zürich, Switzerland.

Celia MA, Bouloutas ET and Zarba RL (1990) A general mass-conservative numerical solution for the unsaturated flow equation. *Water Resources Research*, **26**, 1483–1496.

Chavent G and Jaffre J (1986) *Mathematical Models and Finite Elements for Reservoir Simulation*, North-Holland, Amsterdam.

Cordes C and Kinzelbach W (1992) Continuous groundwater velocity fields and path lines in linear, bilinear, and trilinear finite elements. *Water Resources Research*, **28**, 2903–2911.

Cordes C and Kinzelbach W (1996), Comment on "Application of the mixed hybrid finite element approximation in a groundwater flow model: Luxury or necessity?" by R. Mosé, P. Siegel, P. Ackerer, and G. Chavent. *Water Resources Research*, **32**, 1905–1909.

Dalen V (1979) Simplified finite-element models for reservoir flow problems. *Society of Petroleum Engineers Journal*, **19**, 333–343.

Durlofsky LJ (1993) A triangle based mixed finite-element-finite volume technique for modeling two phase flow through porous media. *Journal of Computational Physics*, **105**, 252–266.

Durlofsky LJ (1994) Accuracy of mixed and control volume finite element approximations to Darcy velocity and related quantities. *Water Resources Research*, **30**, 965–973.

Eymard R, Gallouët T and Joly P (1989) Hybrid finite element techniques for oil recovery simulation. *Computer Methods in Applied Mechanics and Engineering*, **74**, 83–98.

Forsyth PA (1991) A control volume finite element approach to NAPL groundwater contamination. *SIAM Journal on Scientific Computing*, **12**, 1029–1057.

Fumeaux C, Baumann D, Leuchtmann P and Vahldieck R (2004) A generalized local time-step scheme for efficient FVTD simulations in strongly inhomogeneous meshes. *IEEE Transactions on Microwave Theory and Techniques*, **52**, 1067–1076.

Harten A (1983) High resolution schemes for hyperbolic conservation laws. *Journal of Computational Physics*, **49**, 357–393.

Helmig R (1997) *Multi-phase Flow and Transport Processes in the Subsurface*, Springer Verlag, Berlin.

Helmig R and Huber R (1998) Comparison of Galerkin-type discretization techniques for two-phase flow in heterogeneous porous media. *Advances in Water Resources*, **21**, 697–711.

Helmig R and Huber R (1999) Multi-phase flow in heterogeneous porous media: A classical finite element method versus and implicit pressure-explicit saturation-based mixed finite element-finite volume approach. *International Journal for Numerical Methods in Fluids*, **29**, 899–920.

Huber R and Helmig R (2000) Node-centered finite volume discretizations for the numerical simulation of multi-phase flow in heterogeneous porous media. *Computational Geosciences*, **4**, 141–164.

Huyakorn PS and Pinder GF (1978) A new finite element technique for the solution of two-phase flow through porous media. *Advances in Water Resources*, **1**, 285–298.

Huyakorn PS and Pinder GF (1987) *Computational Methods in Subsurface Flow*, Academic Press, New York.

Jenny P, Wolfensteiner C, Lee SH and Dourlofsky LJ (2002) Modeling flow in geometrically complex reservoirs using hexahedral multiblock grids. *SPE Journal*, **7**, 149–157.

Lee SH, Tchelepi HA, Jenny P and DeChant LJ (2002) Implementation of a flux-continuous finite-difference method for stratigraphic hexahedron grids. *SPE Journal*, **7**, 267–277.

Letniowski FW and Forsyth PA (1991) A control volume finite element method for three-dimensional NAPL groundwater contamination. *International Journal for Numerical Methods in Fluids*, **13**, 955–970.

Lachassagne P, Ledoux E and de Marsily G (1989) Evaluation of hydrogeological parameters in heterogeneous porous media. In: *Groundwater Management: Quantity and Quality (Proceedings of the Benidorm Symposium, October 1989)* IAHS Publications, **188**, 3–18.

Matthäi SK and Roberts SG (1996) The influence of fault permeability on single phase fluid flow near fault-sand intersections: Results from steady state high-resolution models of pressure-driven fluid flow. *AAPG Bulletin*, **80**, 1763–1779.

Matthäi SK, Aydin A, Pollard DD and Roberts SG (1998) Numerical simulation of departures from radial drawdown in a faulted sandstone reservoir with joints and deformation bands. In: *Faulting, Fault Sealing and Fluid Flow in Hydrocarbon Reservoirs* (eds. G Jones, QJ Fisher and RJ Knipe) Geological Society of London Special Publications, **147**, 157–191.

Matthäi SK, Geiger S and Roberts SG (2001) *Complex Systems Platform: CSP3D3.0: user's guide*. http://e-collection.ethbib.ethz.ch/show?type =bericht&nr=239, Eidgenössische Technische Hochschule Zürich, Switzerland.

Matthäi SK (2003) Fluid flow and (reactive) transport in fractured and faulted rock. *Journal of Geochemical Exploration*, **78-79**, 179–182.

Matthäi SK and Belayneh M (2004) Fluid flow partitioning between fractures and a permeable rock matrix. *Geophysical Research Letters*, **31**, L07602.

Mosé P, Siegel P, Ackerer P and Chavent G (1994) Application of the mixed hybrid finite element approximation in a groundwater flow model: Luxury or necessity? *Water Resources Research*, **30**, 3001–3012.

Narasimhan TN and Witherspoon PA (1976) An integrated finite difference method for analyzing fluid flow in porous media. *Water Resources Research*, **12**, 57–64.

Phillips OM (1991) *Flow and Reactions in Permeable Rocks*. Cambridge University Press, Cambridge, U.K.

Pruess K (1991) *TOUGH2 - A General Purpose Numerical Simulator for Multiphase Fluid and Heat Flow*, Lawrence Berkeley Laboratory Report, LBL–29400, Berkeley, CA.

Roberts SG and Matthäi SK (1996) High resolution potential flow methods for oil exploration. In: *Computational Techniques and Applications: CTAC95*, World Scientific Press, 677–684.

Shewchuk JR (2002) Delaunay refinement algorithms for triangular mesh generation *Computational Geometry – Theory and Application*, **22**, 21–74

Spivak S, Price HS and Settari A (1977) Solution of the equations for multidimensional, two-phase, immiscible flow by variational methods. *Society of Petroleum Engineers Journal*, **17**, 27–41.

Stüben K (2001) A review of algebraic multigrid. *Journal of Computational and Applied Mathematics*, **128**, 281–309.

Sweby PK (1984) High resolution schemes using flux limiters for hyperbolic conservation laws. *SIAM Journal on Numerical Analysis*, **21**, 995–1011.

Van Genuchten MT (1980) A closed-form equation for predicting the hydraulic conductivity of unsaturated soils. *Soil Science Society of America Journal*, **44**, 892–898.

Zienkiewicz OC and Taylor RL (2000), *The Finite Element Method*, 5th edn. Butterworth-Heinemann, Oxford.

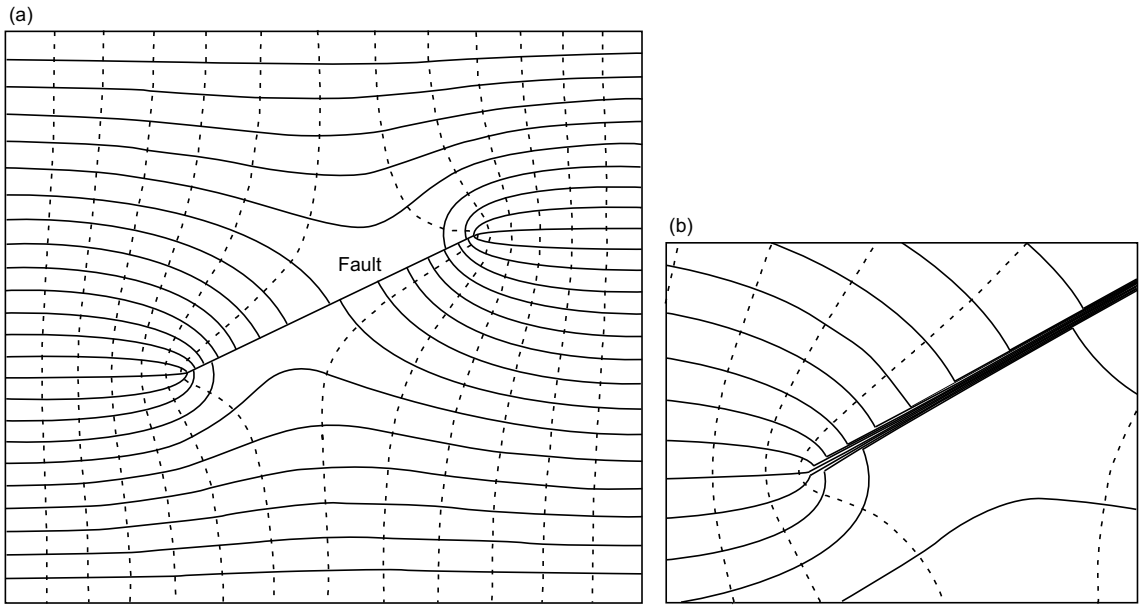

Figure 1: Fluid pressure contours (dashed lines) and stream lines (bold lines) in a rock matrix (500 × 450 meters) with a highly permeable fault zone (approximately 50 cm wide), after Phillips (1991). The permeability of the fault zone is 5 orders of magnitude higher than the matrix permeability and fluid velocities vary up to 5 orders of magnitude. Due to its high permeability, fluid flow is focused into the fault zone (a). Flow is fastest where the fluid pressure contours have the closest spacing, i.e. at the tip of the fault (b)

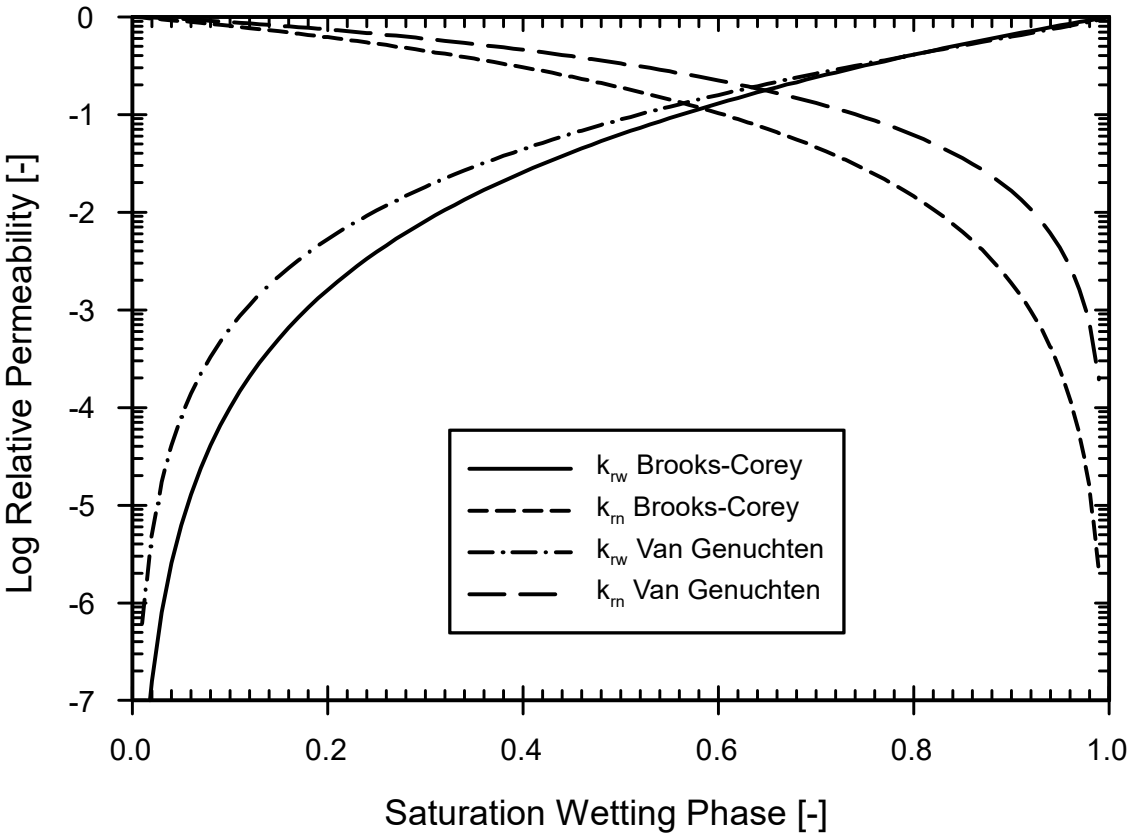

Figure 2: Relative permeability curves as a function of the saturation of the wetting phase for the Brooks-Corey model and the Van Genuchten model with input parameters of 2 and 5, respectively. Residual saturations are 0 in both models.

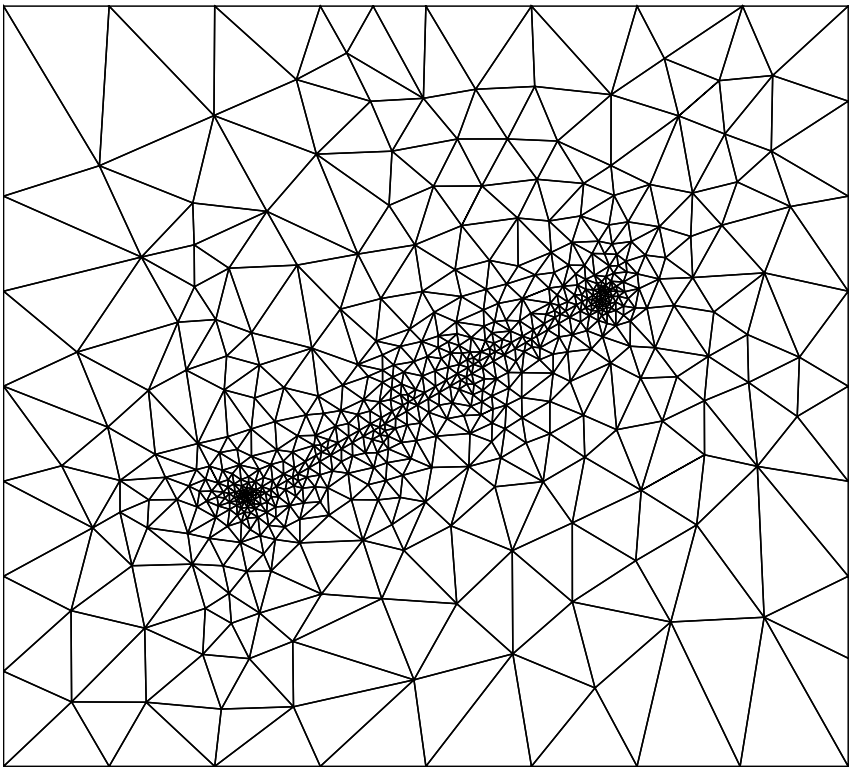

Figure 3: Triangular finite element mesh of the geometry depicted in Figure 1.

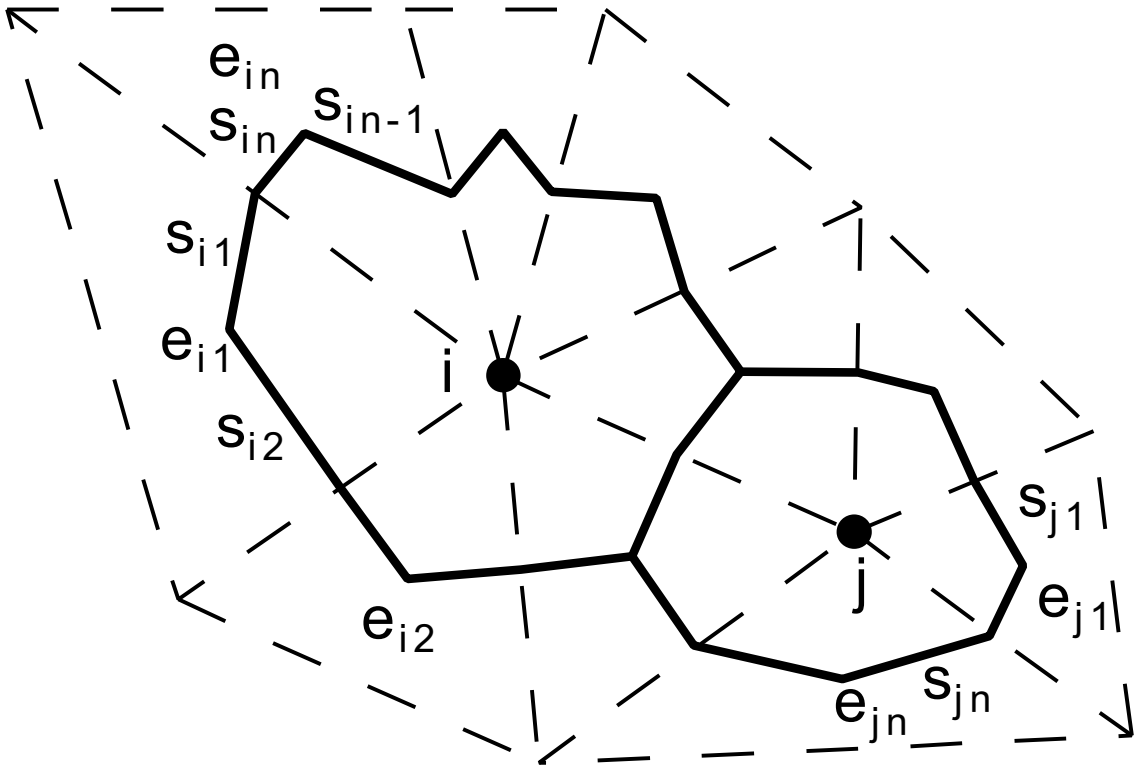

Figure 4: Node-centered finite volumes at nodes i and j with triangular finite elements e_{i1} - e_{in} (e_{j1} - e_{jn}, respectively) and segments s_{i1} - s_{in} (s_{j1} - s_{in}, respectively).

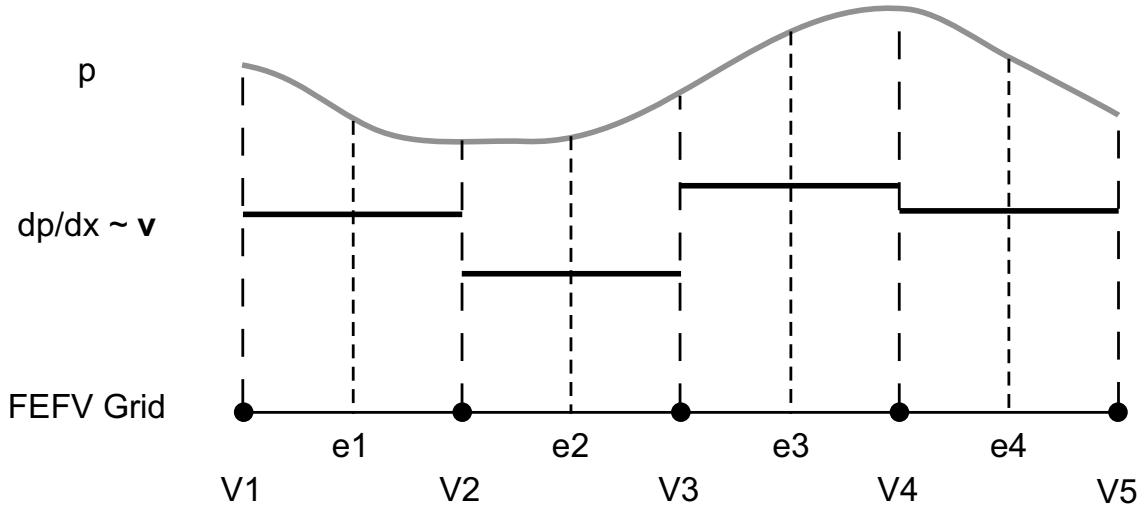

Figure 5: One-dimensional uniform finite element – finite volume grid showing the flux-continuity across boundaries of adjacent finite volumes. The long dashed lines are the boundaries between four finite elements e. The short dashed lines are the boundaries, i.e. finite volume segments, between five node-centered finite volumes V. The run of the fluid pressure p is shown by the gray line. The derivative dp/dx, which is proportional to the fluid velocity $\mathbf{v}$, is shown by the black horizontal lines. For linear interpolation functions Φ, dp/dx is constant and continuous across each finite volume segment but discontinuous across two neighboring finite elements. Integration of the segment flux, i.e. the product of velocity, normal vector, and segment length, over the surface of the finite volume conserves mass on the node-centered finite volume.

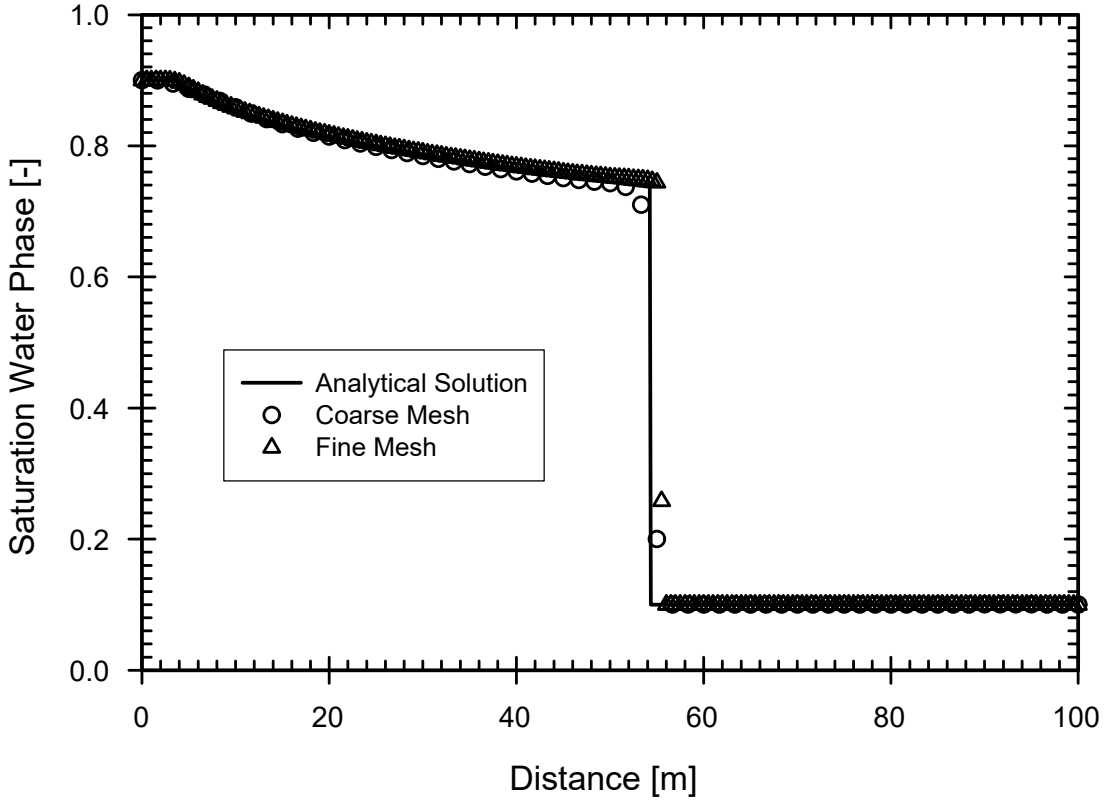

Figure 6: Comparison of the pseudo one-dimensional numerical solution for a coarse and fine mesh (60 nodes and 200 in x-direction, respectively) to the analytical solution of the Buckley-Leverett problem. The water phase displaces the oil phase in a homogeneous porous media. Snapshot is taken after 105 days.

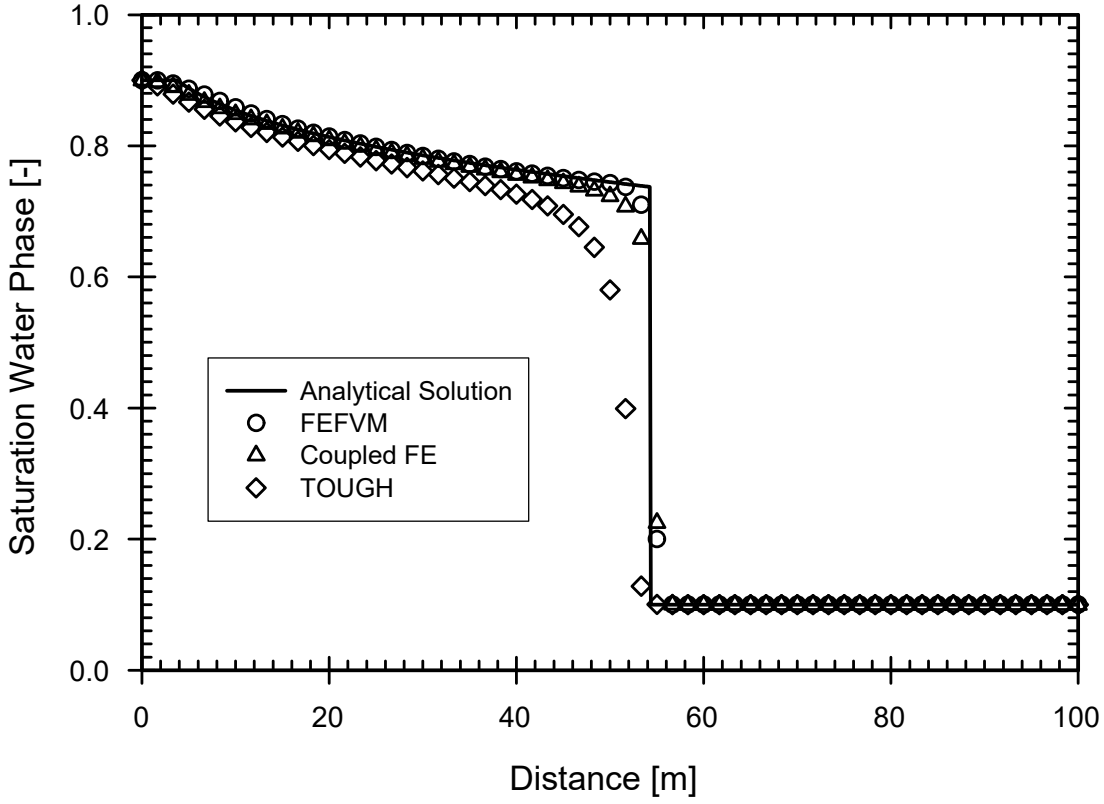

Figure 7: Comparison of solutions for the Buckley-Leverett problem for different solution methods on the coarse mesh (60 nodes in x-direction). The water phase displaces the oil phase in a homogeneous porous media. Snapshot is taken after 105 days.

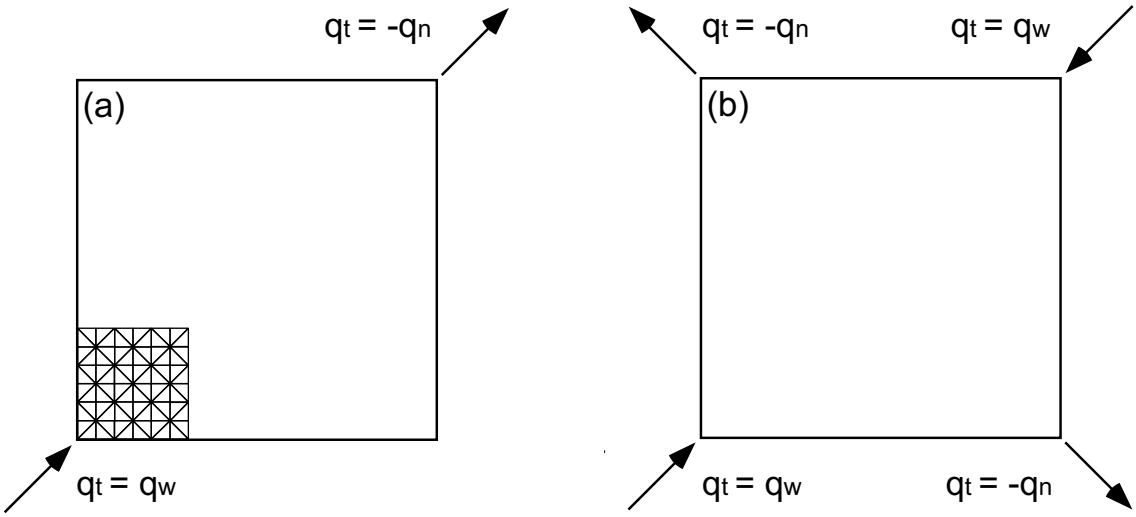

Figure 8: Setup of the five-spot waterflood problem with part of the triangular finite element mesh (not to scale). In case 1, water is injected in the lower left corner, while oil is extracted in the upper right corner (a). Flow is diagonal to the grid. In case 2, water is injected in the lower left and upper right corners, while oil is extracted in the lower right and upper left corners (b). Flow is parallel to the grid. Dimensions are 100×100 meters.

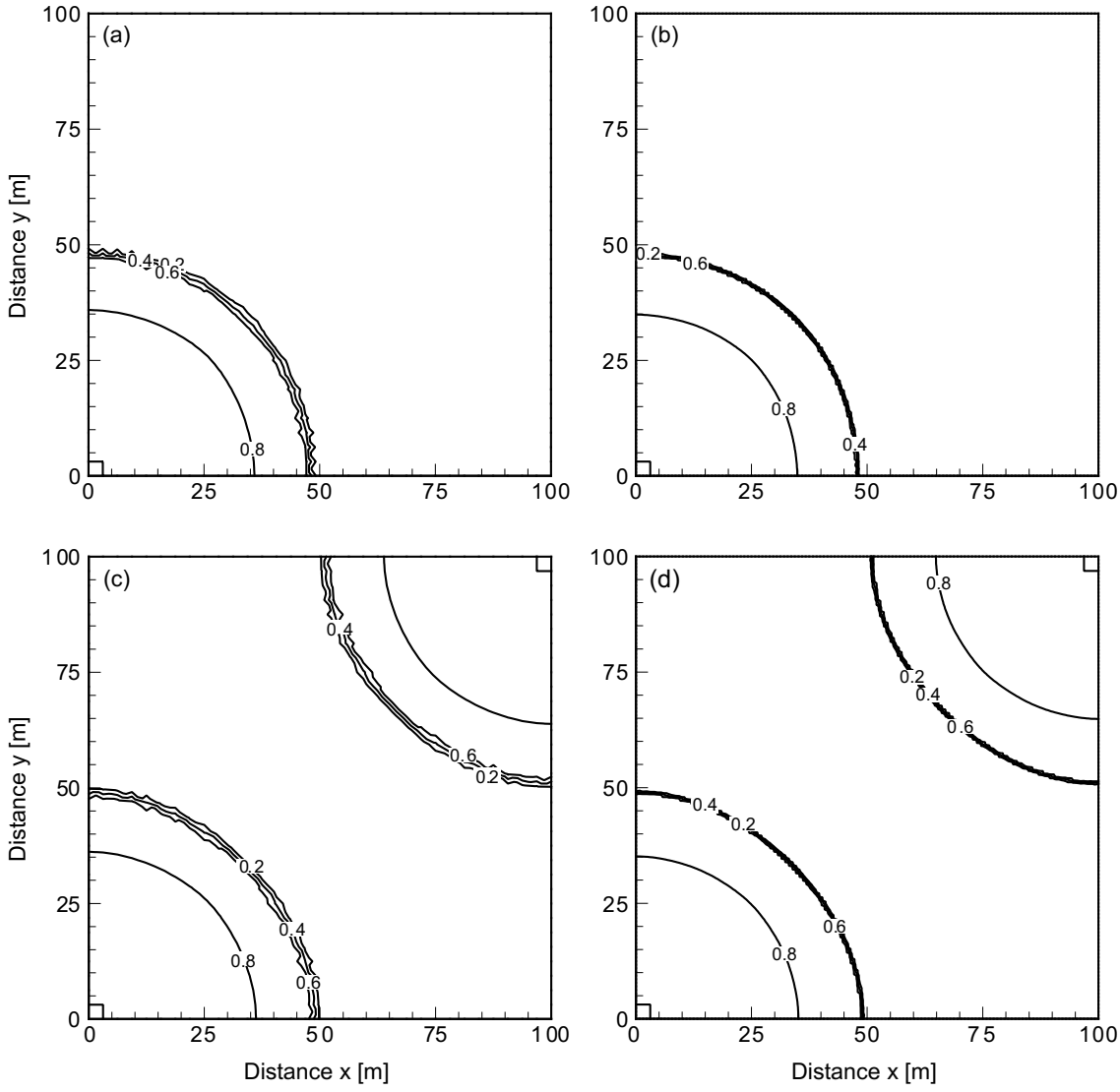

Figure 9: Numerical solution for the five-spot waterflood problem for a coarse (a,c) and fine (b,d) finite element mesh, respectively. Contours show the water saturation after 0.015 PVI. In cases (a) and (b), water is injected in the lower left corner, while oil is extracted in the upper right corner. Here, flow is diagonal to the grid. In cases (c) and (d), water is injected in the lower left and upper right corners, while oil is extracted in the lower right and upper left corners. Here, flow is parallel to the grid.

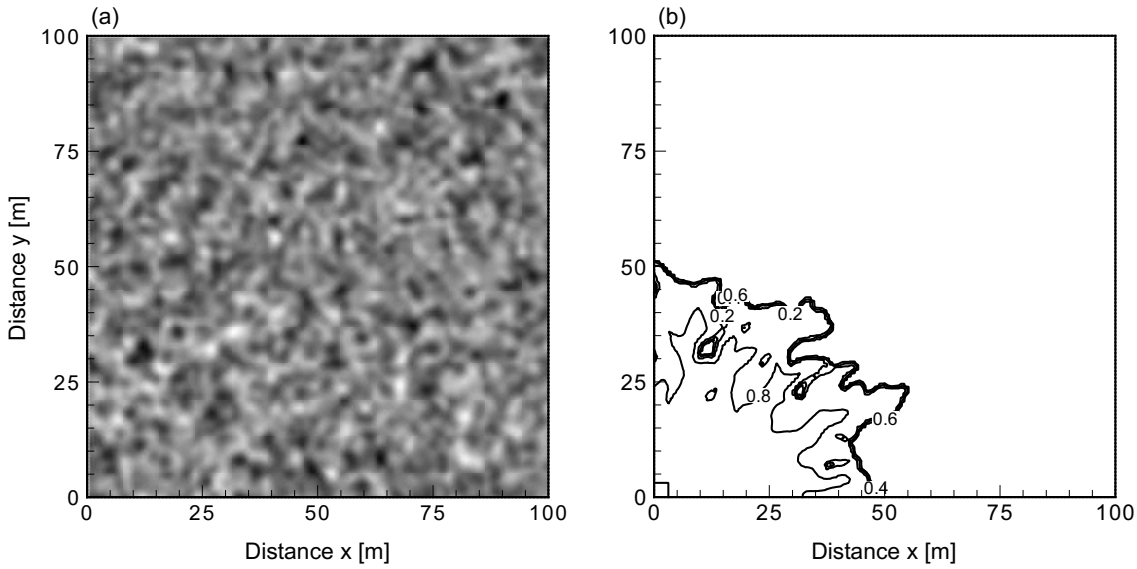

Figure 10: Permeability field (darkest values correspond to $\mathbf{k} = 10^{-14}$ m^2, brightest values to $\mathbf{k} = 10^{-10}$ m^2) (a) and numerical solution showing the contours of the water saturation after 0.015 PVI (b).

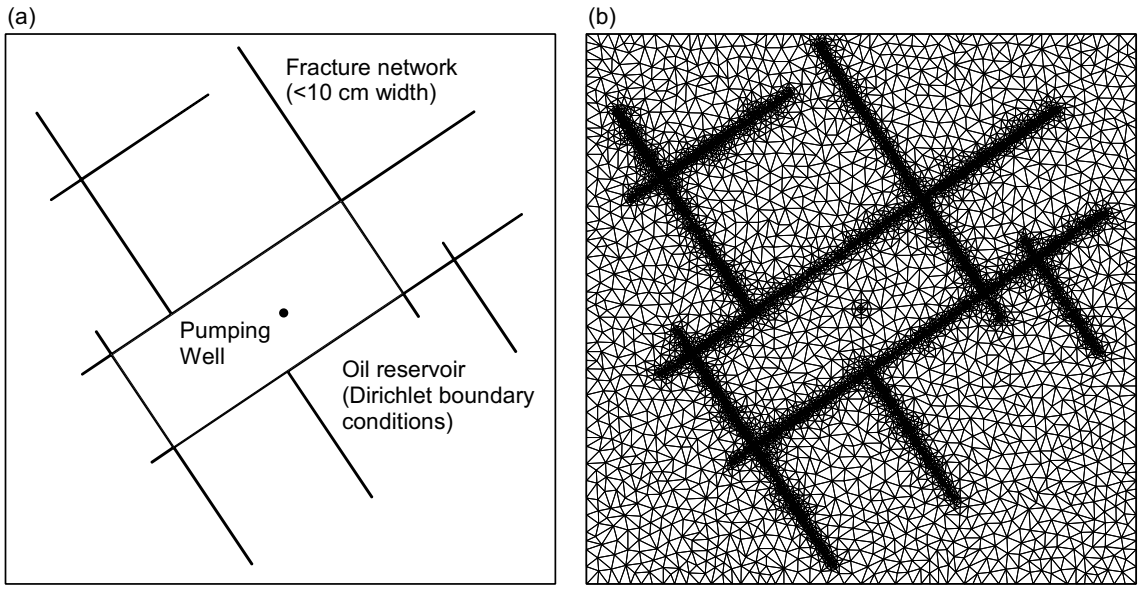

Figure 11: Model setup (plan view) for the simulation of pumping in a reservoir with an interconnected fracture system (a) and finite element triangulation (b). Note that triangles within the fractures and their immediate vicinity are so small that they are not resolved on the model scale and appear as bold black lines. Model dimensions are 50×50 meters.

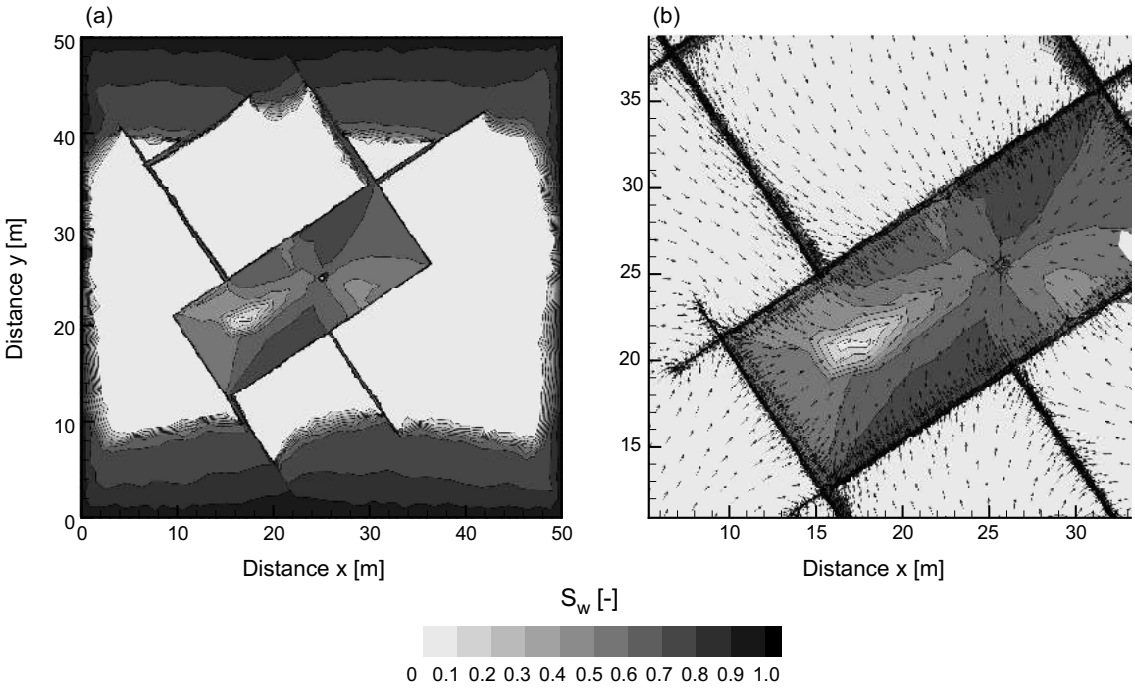

Figure 12: Contours of water saturation after 10 PVE (a) and close-up of the model in the area of the well (b). Arrows depict direction of flow. Note how flow is focused into and out of the fractures due to the deviations in fluid pressure from the radial drawdown.

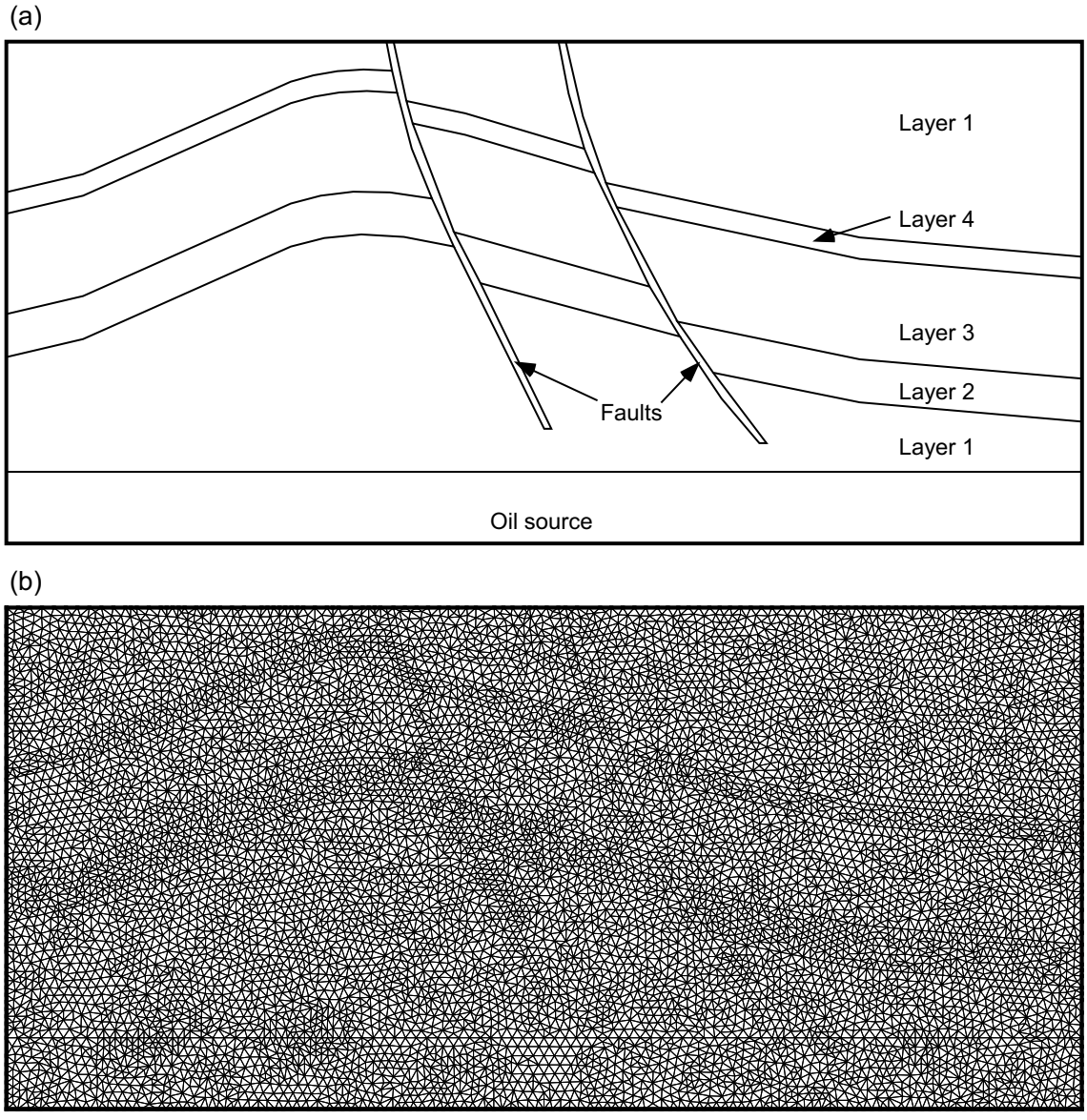

Figure 13: Structure of the idealized faulted sedimentary basin with its lithologies (a) and the corresponding triangular finite element mesh (b). The properties of the different lithologies are listed in Table 2. The model was discretized by 17,545 triangular finite elements with element areas varying from 18 to 108 m^2. Model dimensions are 1500×700 meters.

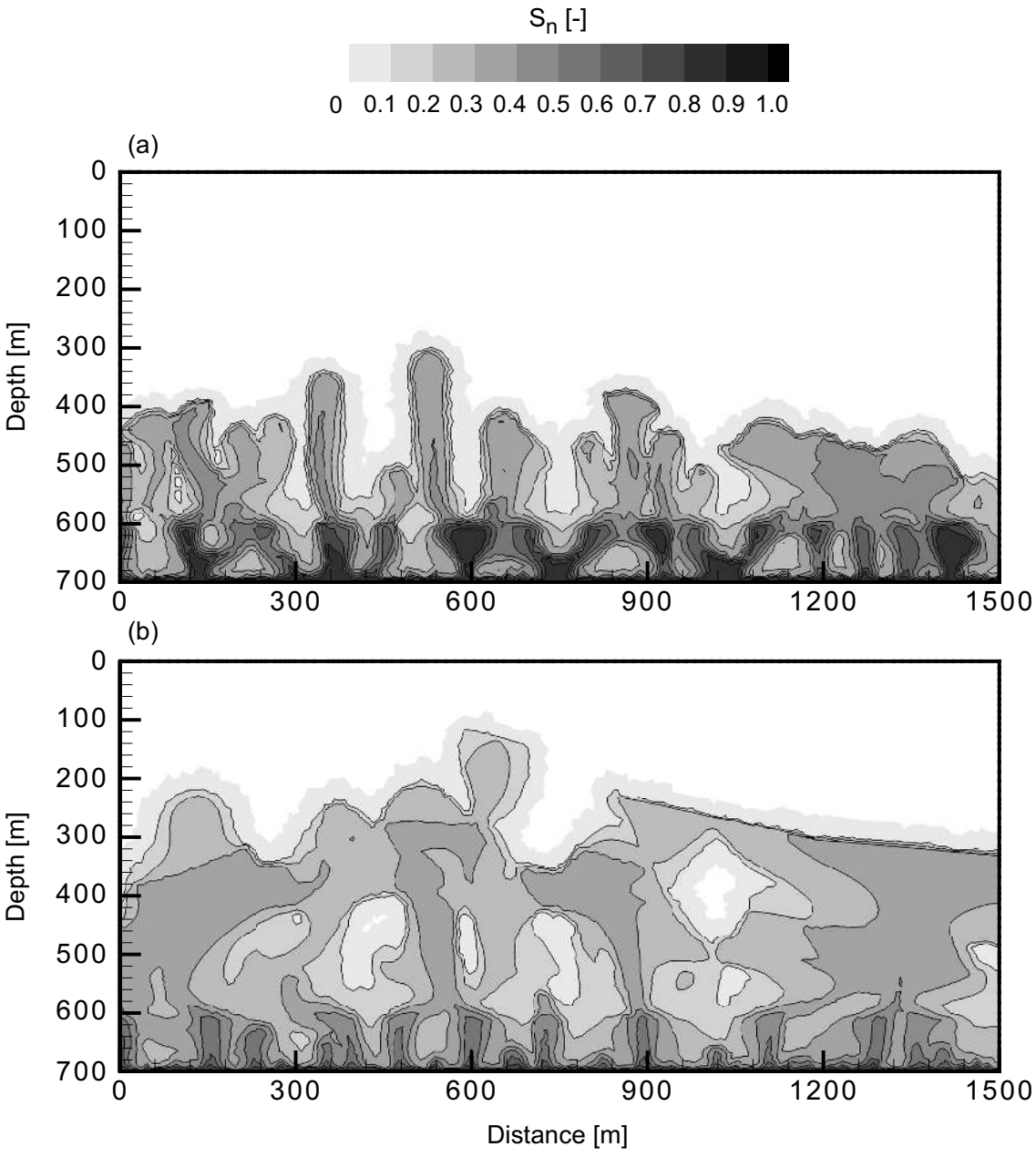

Figure 14: Oil saturation after 2000 years (a) and 4000 years (b).

Scheme	Δt [d]	Runtime [min]	Total iterations	Avg. iterations
Picard	0.1	1:55	6980	4.65
Picard	0.33	1:18	4195	9.22
Newton	0.1	4:07	6057	4.09
Newton	0.33	2:13	3377	7.35
FEFVM	0.1	0:16	-	-

Table 1: Runtime properties for fully coupled finite element and FEFVM approaches for the Buckley-Leverett problem using the coarse mesh. Picard and Newton iteration schemes were employed in the fully coupled finite element formulation. Simulations were carried out on a Pentium IV processor with 2.6 GHz. Runtime properties for TOUGH simulations are not shown because these runs were carried out on a Sun workstation.

Layer	$\log \mathbf{k}$ [m^2]	ϕ [-]	BC [-]	p_e [Pa]	S_{wr} [-]	S_{nr} [-]
Oil source	-14.3	0.2	2.5	5000.0	0.05	0.15
Layer 1	-13.0	0.2	2.5	1000.0	0.05	0.15
Layer 2	-14.0	0.15	2.0	3000.0	0.07	0.17
Layer 3	-12.3	0.22	3.0	750.0	0.05	0.10
Layer 4	-16.0	0.1	1.8	10000.0	0.09	0.22
Fault	-12.0	1.0	1.0	0.0	0.01	0.07

Table 2: Properties of the different rock units of the sedimentary basin depicted in Figure 13. BC denotes the Brooks-Corey parameter, p_e the capillary entry pressure, and S_{wr} and S_{nr} the residual saturations of the wetting and non-wetting phase, respectively.

Symbol	Parameter	Unit
$\mathbf{a}$	Gradient vector	[m^{-1}]
A	Finite volume area	[m^2]
c_t	Total system compressibility	[Pa^{-1}]
e	Element	[–]
f	Fractional flow function	[–]
$\mathbf{g}$	Gravitational acceleration vector	[kg m s^{-2}]
i, j	Indices over nodes	[–]
k_r	Relative permeability function	[–]
$\mathbf{k}$	Permeability tensor	[m^2]
n	Non-wetting (oil) phase	[–]
$\mathbf{n}$	Normal vector	[–]
p	Fluid pressure	[Pa]
q	Fluid source/sink	[m^3 s^{-1}]
r	Limiter value	[–]
s	Finite volume segment	[–]
S	Saturation	[–]
t	Time	[s]
t	As subscript: Total (oil + water) property	[–]
$\mathbf{v}$	Fluid velocity	[m s^{-1}]
V	Finite volume	[–]
w	Wetting (water) phase	[–]
$\mathbf{x}$	Coordinate vector	[m]
α	Phase	[–]
Δ	Increment	[–]
λ	Mobility	[Pa s^{-1}]
μ	Viscosity	[Pa s^{-1}]
ϕ	Porosity	[–]
Φ	Basis or interpolation function	[–]
Ψ	Limiter function	[–]
ρ	Density	[kg m^{-3}]
Ω	Computational domain	[–]

Table 3: List of used symbols and corresponding units.